

# The converging gas flow around the infrared dark cloud G28.37

H. Beuther<sup>1</sup>, C. Gieser<sup>1</sup>, H. Linz<sup>1</sup>, Q. Zhang<sup>2</sup>, S. Feng<sup>3</sup>, A. Ahmadi<sup>4</sup>, J.D. Soler<sup>5</sup>, D. Semenov<sup>6,1</sup>, M.R.A. Wells<sup>1</sup>, and S. Reyes-Reyes<sup>1</sup>

<sup>1</sup> Max Planck Institute for Astronomy, Königstuhl 17, 69117 Heidelberg, Germany, e-mail: name@mpia.de

<sup>2</sup> Harvard-Smithsonian Center for Astrophysics, 160 Garden St, Cambridge, MA 02420, USA

<sup>3</sup> Department of Astronomy, Xiamen University, Zengcuoan West Road, Xiamen, 361005, People's Republic of China

<sup>4</sup> ASTRON, Netherlands Institute for Radio Astronomy, Dwingeloo, the Netherlands

<sup>5</sup> Department of Astrophysics, University of Vienna, Türkenschanzstrasse 17, 1180 Vienna, Austria

<sup>6</sup> Zentrum für Astronomie der Universität Heidelberg, Institut für Theoretische Astrophysik, Albert-Ueberle-Str. 2, 69120 Heidelberg, Germany

Version of January 13, 2026

## ABSTRACT

**Context.** How dense clouds and star-forming regions form out of the dynamical interstellar medium is at the heart of star formation research.

**Aims.** The G28.37+0.07 star-forming region is a prototypical infrared dark cloud (IRDC) located at the interface of a converging gas flow. This study characterizes the properties of this dynamic gas flow.

**Methods.** Combining data from the Northern Extended Millimeter Array (NOEMA) with single-dish data from the IRAM 30 m observatory, we mapped large spatial scales ( $\sim 81$  pc $^2$ ) at high angular resolution ( $7.0'' \times 2.6''$  corresponding  $\sim 2.3 \times 10^4$  au or  $\sim 0.1$  pc) down to core scales. The spectral setup in the 3 mm band covers many spectral lines as well as the continuum emission.

**Results.** The data clearly reveal the proposed west-east converging gas flow in all observed dense gas tracers. We estimate a mass-flow rate along that flow around  $10^{-3} M_{\odot} \text{yr}^{-1}$ . Comparing these west-east flow rates to infall rates toward sources along the line of sight, the gas flow rates are roughly a factor of 25 greater than those along the line of sight (roughly perpendicular to the west-east flow). This confirms the dominance of longitudinal motions along the converging gas flow in this region. For comparison, in the main north-south IRDC formed by the west-east converging gas flow, infall rates along the line of sight are about an order of magnitude greater than those along the west-east flow. In addition to the kinematic analysis, a comparison of CH<sub>3</sub>CN-derived gas temperatures with Herschel-derived dust temperatures typically show higher gas temperatures toward high-density sources. We discuss whether mechanical heating from the conversion of the flow's kinetic energy into thermal energy may explain some of the observed temperature differences.

**Conclusions.** Our analysis of the G28.37+0.07 converging gas flow shows that such structures can indeed form and feed typical high-mass star-forming regions in the Milky Way. The differences between flow rates along the converging flow, perpendicular to it, and toward the sources at the IRDC center indicate that at the interfaces of converging gas flows – where most of the active star formation takes place – originally more directed gas flows can convert into multidirectional infall motions.

**Key words.** Stars: formation – ISM: clouds – ISM: kinematics and dynamic – ISM: individual objects: G28.37+0.07

## 1. Introduction

The current paradigm for molecular cloud formation and the subsequent collapse of star-forming regions into individual stars and clusters views the entire process as a hierarchical gas flow from large to small scales (e.g., Vázquez-Semadeni et al. 2000; Vázquez-Semadeni et al. 2011, 2017, 2019; Heitsch et al. 2005; Glover & Mac Low 2007; Banerjee et al. 2009; Ibáñez-Mejía et al. 2017; Motte et al. 2018; Ballesteros-Paredes et al. 2018; Padoan et al. 2020; Pineda et al. 2023; Hacar et al. 2023; Beuther et al. 2025a). While this picture is theoretically appealing, observational signatures are still scarce, with notable exceptions presented in Schneider et al. (2010), Csengeri et al. (2011a,b), Hennemann et al. (2012), Tackenberg et al. (2014), Hacar et al. (2017), Beuther et al. (2020), Kido et al. (2025), and Gieser et al. (2025). Certainly, observational studies following the gas flow from the largest cloud scales – potentially still atomic – to the smallest core scales, where individual or multiple stars form, barely exist. These kinematic flows are directly associated with the fragmentation of clouds as well as the chemical evolution of

the interstellar medium (ISM) and star-forming cores. A central goal in molecular cloud and star formation research is to characterize the entire gas flow process, the fragmentation, and the chemical evolution of the material in depth. This requires covering a broad range of spatial scales as well as gas densities.

To address these topics, we embarked on a concerted effort to investigate the prototypical infrared dark cloud (IRDC) G28.37+0.07 (G28 in the following) from the atomic gas at large scales ( $> 20$  pc, Beuther et al. 2020) via dense gas studies at typical single-dish resolutions (Tackenberg et al., 2014) down to scales of several thousand au only reachable with interferometers such as NOEMA.

The star formation region G28 at a distance of 4.7 kpc is a large cloud complex where the innermost region is the well-known IRDC G28 (e.g., Pillai et al. 2006; Rathborne et al. 2006; Wang et al. 2008; Butler & Tan 2012; Tan et al. 2013; Tackenberg et al. 2014; Kainulainen & Tan 2013; Zhang et al. 2015; Feng et al. 2016; Kong et al. 2019; Beuther et al. 2020; Barnes et al. 2023; Law et al. 2024; Liu et al. 2024). Infrared data from the Spitzer satellite (Fig. 1 left panel; Churchwell

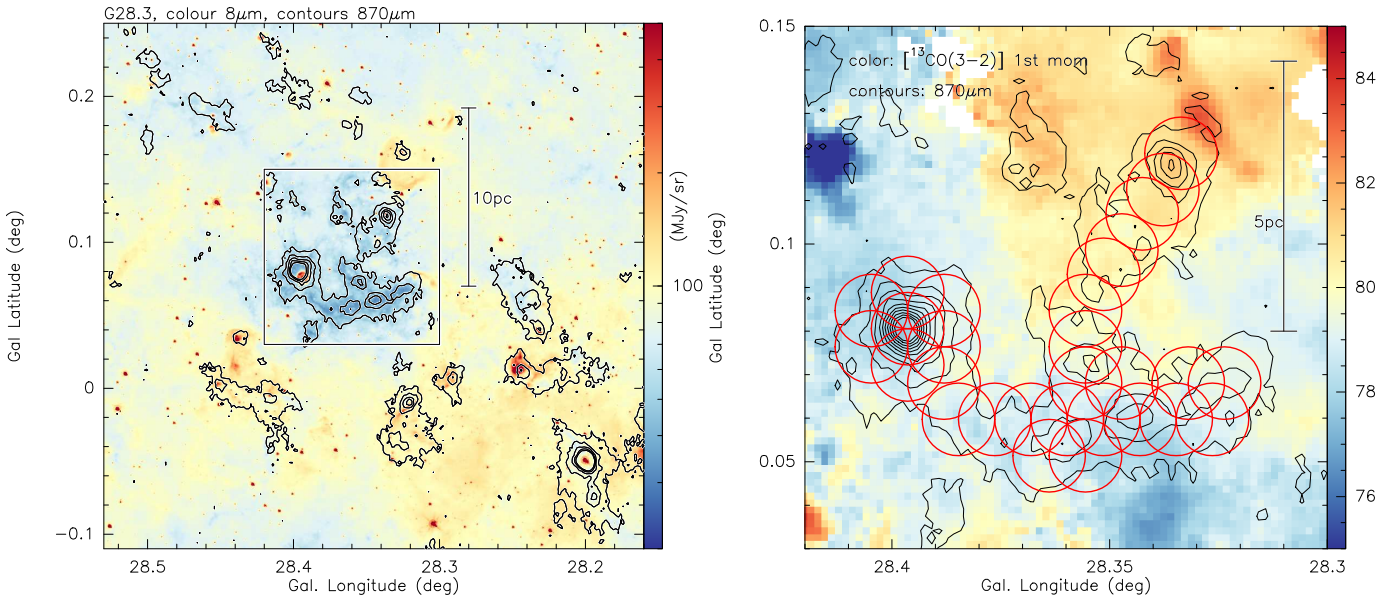


**Fig. 1.** Overview of the G28 region. Left panel: Color scale showing GLIMPSE 8  $\mu\text{m}$  emission (Churchwell et al., 2009) for the G28 IRDC. The contours show the corresponding ATLASGAL 870  $\mu\text{m}$  dust continuum emission, starting at  $4\sigma$  (200 mJy beam $^{-1}$ ) (Schuller et al., 2009) and continuing in  $8\sigma$  steps. The box outlines the area shown to the right. Right panel: Zoom into the G28 target region. The color scale presents the velocity field (first moment) observed in  $^{13}\text{CO}(3-2)$  with APEX (Beuther et al., 2020). The contours show the 870  $\mu\text{m}$  continuum emission from the ATLASGAL survey (Schuller et al., 2009). The red circles outline the observed NOEMA mosaic. A scale bar is shown to the right in both panels.

et al. 2009) show that filamentary extinction structures extend from the large-scale outskirts down to the cloud’s central region. Observations of the dense gas in  $\text{N}_2\text{H}^+$  indicate that the region is in a stage of global collapse (Tackenberg et al., 2014). Different evolutionary stages of star formation activity exist throughout the cloud from almost quiescent clumps to bright mid-infrared high-mass protostellar objects (e.g., Pillai et al. 2006; Wang et al. 2008; Butler & Tan 2012; Feng et al. 2016). This makes the G28 complex an ideal candidate for investigating the kinematic and chemical properties during cloud and star formation in a uniform way.

To investigate the kinematics on large scales ( $>30$  pc) from the atomic and molecular envelopes of the IRDC, Beuther et al. (2020) made use of the HI self-absorption (HISA) data from the THOR survey (Beuther et al., 2016),  $^{13}\text{CO}(1-0)$  molecular line data from the Galactic Ring survey (Jackson et al., 2006), as well as APEX observations in the atomic [CI] and  $^{13}\text{CO}(3-2)$  emission lines. This combined dataset shows velocity gradients across the entire cloud complex (Fig. 1 right panel) that are interpreted as converging gas flows with flow rates between  $10^{-5}$  and  $10^{-4} \text{ M}_\odot \text{yr}^{-1}$  (Beuther et al., 2020).

How do these large-scale characteristics relate to the small-scale kinematics, fragmentation, and chemical evolution of the central G28 IRDC? We address these topics here via a NOEMA (Northern Extended Millimeter Array) mosaic study of the central G28 IRDC.

## 2. Observations

### 2.1. The Northern Extended Millimeter Array (NOEMA)

The G28 IRDC was observed between June and October 2019 with NOEMA in the 3 mm band with nine antennas in the array. The two compact configurations, D and C, were used, and we observed a 29-field mosaic, as outlined in Figure 1 (right panel). Phase calibration was conducted through regularly interleaved

observations of quasars 1829-106 and 1851+0035. For bandpass calibration, we used the strong quasar 1749+096, and for the flux calibration we observed MWC349. The calibration was conducted in CLIC, and imaging was subsequently performed in MAPPING; both programs are part of the GILDAS software suite<sup>1</sup>. The phase center of the mosaic is Right Ascension (J2000.0) 18:42:45.65, Declination (J2000.0)  $-04:01:47.75$ . The rest velocity of the region is  $v_{\text{LSR}} = 79.5 \text{ km s}^{-1}$  (e.g., Beuther et al. 2020). The 3 mm tuning covered a broad bandpass between 70.22 to 78.33 GHz in the lower sideband and between 85.71 to 93.82 GHz in the upper sideband. While the spectral resolution over the entire bandpass is 2 MHz, the polyfix correlator is extremely flexible by accommodating many high-spectral resolution sub-windows at a resolution of 62.5 kHz. For the analysis conducted in this paper, we restricted ourselves to a suite of lines tracing different densities, deuterated and non-deuterated species, as well as shock tracers. The spectral lines and parameters are listed in Table 1.

While the spectral line data were imaged after complementing the short spacings from the IRAM 30 m observatory (see the following subsections), continuum short spacing observations for this region do not exist, and we imaged NOEMA-only data. After excluding the 29 strongest spectral lines, the entire lower and upper sideband (LSB and USB) data were collapsed into LSB and USB continuum data and then merged into double-sideband (DSB) continuum data used in the following analysis. The final DSB continuum was created from  $\sim 15.69$  GHz of the bandpass. Using natural weighting and hogbom cleaning, the resulting beam size and rms are  $7.0'' \times 2.6''$  and  $0.1 \text{ mJy beam}^{-1}$ .

### 2.2. IRAM 30 m

To complement the missing short spacings of the spectral line data and obtain large-scale information, we observed the same

<sup>1</sup> <http://www.iram.fr/IRAMFR/GILDAS>

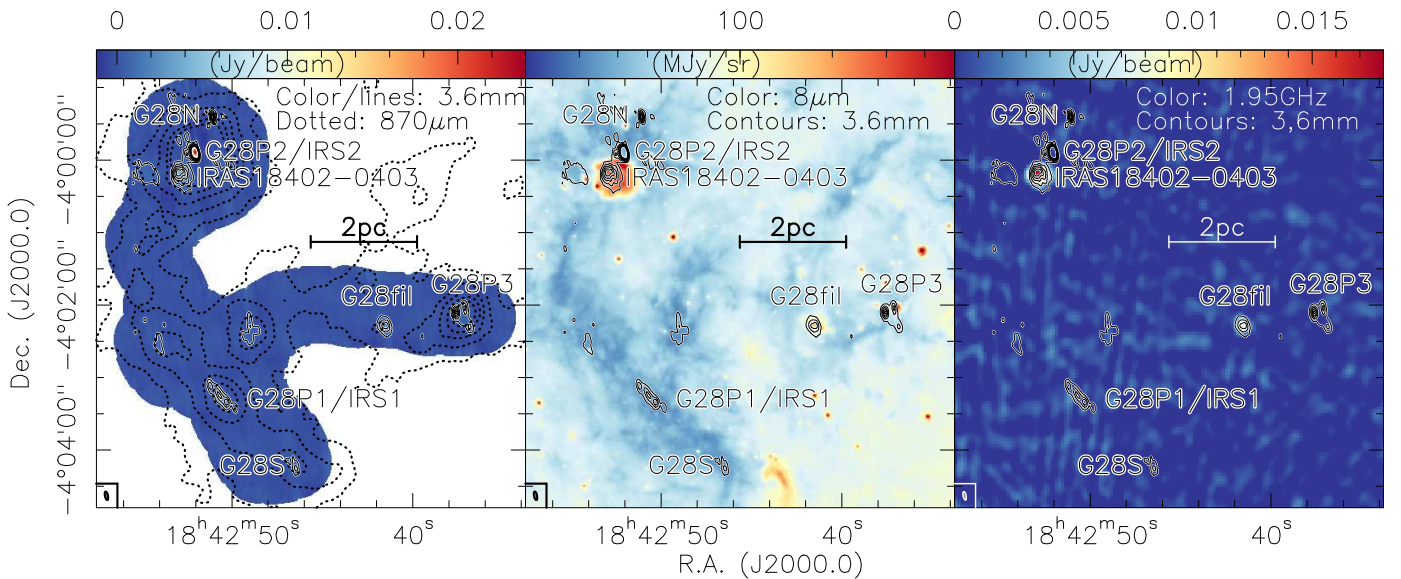


**Fig. 2.** Continuum images of the G28 IRDC. Color scale and solid contours showing the NOEMA 3 mm continuum emission. Contour levels range from 0.4 to 1.6 mJy beam $^{-1}$  ( $1\sigma \sim 0.1$  mJy beam $^{-1}$ ). The dotted contours show 870  $\mu$ m single-dish continuum data (ATLASGAL, Schuller et al. 2009) starting at 0.15 Jy beam $^{-1}$  and continuing in steps of 0.3 Jy beam $^{-1}$  up to 1.5 Jy beam $^{-1}$  ( $1\sigma \sim 0.05$  Jy beam $^{-1}$ ). Middle: Color scale showing the Spitzer 8  $\mu$ m emission (2'' resolution, Churchwell et al. 2009) with 3 mm emission overlaid as contours. Right: Color scale showing the 1.95 GHz continuum emission from the THOR survey (10.6''  $\times$  9.0' resolution, Beuther et al. 2016; Wang et al. 2020) with 3 mm emission overlaid as contours. All panels show a scale bar and the NOEMA synthesized beam. Source labels follow Carey et al. (2000), Wang et al. (2008); G28N and G28fil are newly labeled here.

**Table 1.** Line parameters

line	freq. (GHz)	$1\sigma_{30m}$ (Jy beam)	$1\sigma_{\text{merged}}$ (mJy beam)	beam ('')	$n_{\text{eff}}^a$ ( $\text{cm}^3$ )
continuum	82.02	–	0.1	7.0 $\times$ 2.6	
DCO <sup>+</sup> (1–0)	72.039	0.187	14.5	8.3 $\times$ 3.2	
SO <sub>2</sub> (6 <sub>0.6</sub> – 5 <sub>1.5</sub> )	72.758	0.155	13.0	8.2 $\times$ 3.1	
H <sub>2</sub> CO(1 <sub>0.1</sub> – 0 <sub>0.0</sub> )	72.838	0.161	9.9	8.2 $\times$ 3.1	2.6
CH <sub>3</sub> CN(4 <sub>0</sub> – 3 <sub>0</sub> )	73.590	0.144	9.5	8.2 $\times$ 3.1	37
DNC(1–0)	76.306	0.111	9.9	8.0 $\times$ 3.0	
NH <sub>2</sub> D(1–0)	85.926	–	7.5	7.0 $\times$ 2.5	
H <sup>13</sup> CO <sup>+</sup> (1–0)	86.754	0.165	7.6	7.3 $\times$ 2.6	22
SiO(2–1)	86.847	0.149	8.6	7.3 $\times$ 2.6	15 <sup>b</sup>
HCN(1–0)	88.632	0.146	16.1	7.2 $\times$ 2.6	4.5
HCO <sup>+</sup> (1–0)	89.189	0.160	9.5	7.1 $\times$ 2.5	0.5
CH <sub>3</sub> CN(5 <sub>0</sub> – 4 <sub>0</sub> )	91.987	0.148	6.8	7.0 $\times$ 2.5	74
<sup>13</sup> CS(2–1)	92.494	0.126	9.6	6.9 $\times$ 2.5	5.4 <sup>c</sup>
N <sub>2</sub> H <sup>+</sup> (1–0)	93.174	0.146	11.8	6.9 $\times$ 2.5	5.5

Notes: The  $1\sigma$  rms values are for all lines in the merged data at 0.8 km s $^{-1}$  channel width. Only NH<sub>2</sub>D is for the NOEMA-only data. The continuum rms is for NOEMA-only data across the whole bandpass, excluding the strong spectral lines.

<sup>a</sup> Effective densities at 20 K from Shirley (2015).

<sup>b</sup> Critical densities (no effective densities in Shirley (2015)).

<sup>c</sup> Value for CS(1–0) in Shirley (2015).

region in the on-the-fly mode with the IRAM 30 m telescope within project 100-19 between February and July 2020. The region was scanned in Right Ascension and Declination to minimize any artificial striping effects. The beam of the 30 m at 86 GHz is roughly 29''. The FTS200 correlator with 0.2 MHz spectral resolution (corresponding to 0.8 km s $^{-1}$  at 75 GHz) was employed. For the strongest lines, we used the even higher spectral-resolution unit with 50 kHz resolution. In the end, to achieve a homogeneous spectral resolution for all lines, we

used 0.8 km s $^{-1}$  for the single-dish as well as the merged NOEMA+30 m datasets. Following IRAM guidelines, calibration to main beam temperature  $T_{\text{mb}}$  was performed by multiplying the data by the ratio of forward efficiency to beam efficiency  $f_{\text{eff}}/b_{\text{eff}} = 1.17^2$ . The conversion to Jy beam $^{-1}$  was estimated in the Rayleigh-Jeans limit at the respective frequencies taking into account the beam size. This conversion factor was typically around 4.94. The  $1\sigma$  rms values are also reported in Table 1.

### 2.3. Merged data

The merging of the NOEMA and 30 m data was again conducted in MAPPING, and the 30 m data were converted into pseudo-visibilitys via the `uv_SHORT` task. The NOEMA and 30 m data were then imaged together with natural weighting, hogbom cleaning, and 0.8 km s $^{-1}$  channel width. The final rms of the merged data  $1\sigma_{\text{merged}}$  and the resulting beam sizes are reported in Table 1.

## 3. Results

### 3.1. Continuum emission

Fig. 2 presents the new NOEMA 3 mm continuum data compared to the single-dish 870  $\mu$ m data (Schuller et al., 2009), mid-infrared Spitzer 8  $\mu$ m data (Churchwell et al., 2009), and centimeter wavelength 1.95 GHz emission from the THOR survey (Beuther et al., 2016; Wang et al., 2020). The mid-infrared 8  $\mu$ m data clearly show that the long north-south filamentary structure is mainly infrared-dark, indicating the overall youth and high density of the region. Nevertheless, to the north lies the bright infrared and centimeter continuum source IRAS18402-0403, which is clearly in a more advanced evolutionary stage.

<sup>2</sup> <http://www.iram.es/IRAMES/mainWiki/Iram30mEfficiencies>

Directly north of that lies the G28P2/IRS2 source, which is barely detected in the  $8\mu\text{m}$  Spitzer image (but nevertheless hosts an infrared source also detected with JWST; Reyes-Reyes et al. subm. to A&A) and not detected at centimeter wavelengths. Regarding the east-west structure, while partly also infrared-dark, G28fil has infrared and centimeter counterparts toward the west, and G28P3 has an infrared counterpart as well. Hence, while overall young and often classified as a prototypical infrared-dark cloud, the region clearly hosts a diverse range of evolutionary stages. Even the infrared-dark structures are largely not starless; prominent detection of many outflows confirms the presence of active star formation in these regions as well (e.g., Wang et al. 2006, 2012; Feng et al. 2016; Tan et al. 2016; Kong et al. 2019).

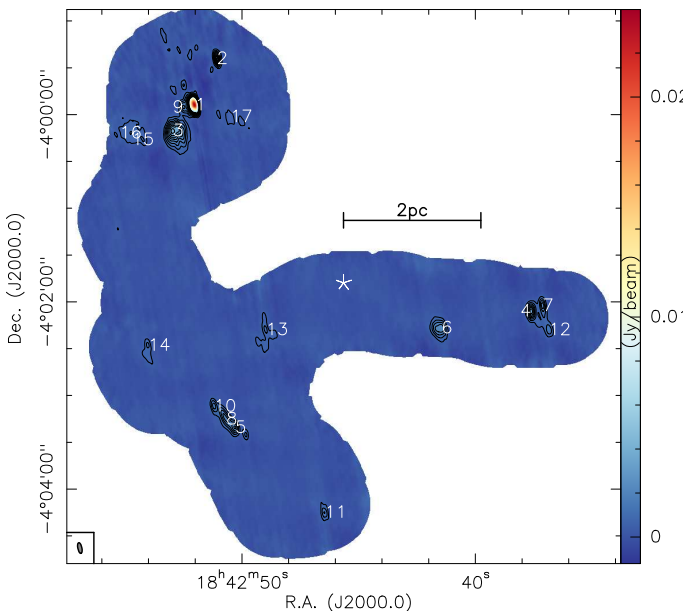


**Fig. 3.** 3.6 mm continuum data with source identifications. The contour levels start at the  $5\sigma$  level ( $0.5\text{ mJy beam}^{-1}$ ) and continue in  $5\sigma$  steps. The sources from the Clumpfind identification are labeled; the star marks the phase-center position for the source offsets in Table 2. A scale bar and the synthesized beam are shown as well.

Using the Clumpfind algorithm (Williams et al., 1994) on the 3.6 mm continuum data, we extracted sources from the region above a  $5\sigma$  threshold. Peak and integrated fluxes are presented in Table 2. The source numbers are sorted in decreasing peak intensities  $S_{\text{peak}}$ , and Fig. 3 presents the respective source number assignments. Assuming optically thin dust continuum emission at a 3.6 mm wavelength, we can estimate the column densities  $N$  and masses  $M$  following Hildebrand (1983) and Schuller et al. (2009). We assumed a gas-to-dust-mass ratio of 150 (Draine, 2011) and a dust opacity  $\kappa = 0.1\text{ cm}^2\text{g}^{-1}$ , extrapolated from Ossenkopf & Henning (1994) to 3.6 mm at densities of  $10^5\text{ cm}^{-3}$ . We did not derive column density and mass estimates for IRAS18402-0403 (source #3) and G28fil (source #6) since free-free emission (Fig. 2, right panel) strongly contaminates the 3.6 mm fluxes.

Regarding the temperatures of the region, we can follow two approaches. On the one hand, the dust temperature map derived by Marsh et al. (2017) from the Herschel far-infrared data reveals temperatures at an angular resolution of  $12''$  toward all sources between 17 and 23 K (Table 2 & Fig. 4). On the other hand, our

spectral setup covers two  $\text{CH}_3\text{CN}$   $k$ -ladders:  $\text{CH}_3\text{CN}(5_k - 4_k)$  and  $\text{CH}_3\text{CN}(4_k - 3_k)$  with  $k$  from 0 to 4. Assuming local thermodynamic equilibrium, both  $k$ -ladders can be fit together to derive a gas temperature map of the region using the XCLASS radiative transfer package (Möller et al., 2017). We assume that the lines originate from one emission component. The noise was evaluated at each pixel and only pixels with signal-to-noise ratio  $\geq 6$  were fit (e.g., Gieser et al. 2021, 2022). Furthermore, high-noise regions corresponding to the noisy areas at the edge of the field of view ( $\geq 0.2\text{ K}$ ) were masked as well. Figure 4 presents a comparison of the derived temperature maps. While the dust temperatures can be estimated for the entire field,  $\text{CH}_3\text{CN}$  is only detected toward the brightest continuum sources and hence is less extended. Nevertheless, where detected, the  $\text{CH}_3\text{CN}$ -derived gas temperatures are consistently higher than those derived from the far-infrared continuum emission. After smoothing the  $\text{CH}_3\text{CN}$  data to the  $12''$  resolution of the Herschel temperature map and running XCLASS on these data again (Fig. 4 right panel), some temperature differences became smaller; nevertheless, for G28P2/IRS2 (source 1) the estimated temperatures still varied by almost a factor of 2. Table 2 lists the source-averaged mean temperatures for the detected sources from the dust,  $\text{CH}_3\text{CN}$ , and smoothed  $\text{CH}_3\text{CN}$  data. We revisit this potential decoupling of gas and dust temperatures in subregions of G28 in Sect. 4.2.

For the mass and column densities, we used both temperatures. Since the dust temperatures are all close to 20 K, we estimated the masses and column densities once for all sources using a single temperature of 20 K. In addition, for sources with  $\text{CH}_3\text{CN}$  detections, we also estimated these parameters using the  $\text{CH}_3\text{CN}$ -derived temperatures at the original resolution, which corresponds to that of the continuum data. All results are listed in Table 2. The source masses derived this way from the 3.6 mm continuum data for the G28 IRDC range broadly from 47 to more than  $1600\text{ M}_\odot$  (or up to  $784\text{ M}_\odot$  when using the  $\text{CH}_3\text{CN}$  temperatures). With the single-dish ATLASGAL  $870\mu\text{m}$  continuum data shown in the left panel of Fig. 2, we can also estimate the total mass of the region. Using the same parameters as above and assuming 20 K once again, with a dust opacity  $\kappa = 1.85\text{ cm}^2\text{g}^{-1}$  at  $870\mu\text{m}$  (Schuller et al., 2009), the total gas mass of the region is  $\sim 1.26 \times 10^4\text{ M}_\odot$  (within a factor of 2 of the Taurus cloud mass, Goldsmith et al. 2008). Comparing this to the total mass of all identified sources from the NOEMA data, we recover roughly 31% of the emission and mass using the interferometer. The column densities cover a similar range from around  $10^{23}\text{ cm}^{-2}$  to roughly  $4 \times 10^{24}\text{ cm}^{-2}$  (or  $\sim 2.0 \times 10^{24}\text{ cm}^{-2}$  when using the  $\text{CH}_3\text{CN}$  temperatures). Estimated effective source radii are larger than  $0.08\text{ pc}$  (or  $> 16500\text{ au}$ ), at the lower end roughly at our spatial resolution limit. For comparison, higher angular resolution dust continuum images for different subregions indicate even more fragmentation at smaller scales (see, e.g., Zhang et al. (2015) and Kong et al. (2019)).

### 3.2. Integrated molecular line emission

In the following, we concentrate on the spectral line emission and the associated kinematic properties of the gas. Fig. 5 shows a compilation of integrated intensity maps for our selected molecular lines at low ( $\sim 29''$ ) and high ( $7'' \times 2.5''$ , Table 1) angular resolutions. Starting with the 30 m data, all the presented molecular lines are well detected in the entire area of  $\sim 9 \times 9\text{ pc}^2$ . While this is not surprising for abundant species such as  $\text{HCO}^+$ ,  $\text{H}_2\text{CO}$ , and  $\text{N}_2\text{H}^+$ , as well as deuterated species such as  $\text{DCO}^+$  and  $\text{DNC}$ , shock tracers such as  $\text{SiO}$  and  $\text{SO}_2$  or higher density tracers such as  $\text{CH}_3\text{CN}$  and  $^{13}\text{CS}$  emit extended emission

**Table 2.** Continuum parameters

#	R.A. (J2000)	Dec. (J2000)	$S_{\text{peak}}$ (mJy beam $^{-1}$ )	$S_{\text{int}}$ (mJy)	$R$ (pc)	$T_{\text{dust}}$ (K)	$T_{\text{CH}_3\text{CN}}$ (K)	$T_{\text{CH}_3\text{CN}}$ (@12'', K)	$M_{20K}$ ( $M_{\odot}$ )	$N_{20K}$ ( $10^{23}\text{cm}^{-2}$ )	$M_{T_{\text{CH}_3\text{CN}}}$ ( $M_{\odot}$ )	$N_{T_{\text{CH}_3\text{CN}}}$ ( $10^{23}\text{cm}^{-2}$ )
1	18:42:52.02	-03:59:54.0	23.97	39.8	0.14	17	41	33	1692	42.9	784	19.9
2	18:42:51.07	-03:59:24.1	5.09	5.6	0.10	17	—	—	237	9.1	—	—
3 <sup>a</sup>	18:42:52.97	-04:00:10.3	4.22	26.7	0.22	19	—	—	—	—	—	—
4	18:42:37.61	-04:02:06.0	3.87	7.2	0.13	22	30	21	309	6.9	199	4.5
5	18:42:50.28	-04:03:20.6	2.62	4.2	0.10	17	24	17	179	4.7	146	3.8
6 <sup>a</sup>	18:42:41.46	-04:02:16.8	2.46	8.4	0.15	20	—	—	—	—	—	—
7	18:42:37.12	-04:02:02.3	2.31	3.8	0.11	23	21	19	159	4.1	151	3.9
8	18:42:50.67	-04:03:15.1	2.18	5.1	0.12	17	22	20	218	3.9	197	3.5
9	18:42:52.49	-03:59:55.2	2.13	4.1	0.11	17	—	—	175	3.8	—	—
10	18:42:51.19	-04:03:07.0	1.73	2.5	0.09	17	—	—	108	3.1	—	—
11	18:42:46.45	-04:04:15.0	1.53	1.9	0.08	17	—	—	79	2.7	—	—
12	18:42:36.86	-04:02:17.8	1.43	2.9	0.11	19	—	—	122	2.6	—	—
13	18:42:48.97	-04:02:17.8	1.24	3.9	0.14	17	26	22	166	2.2	125	1.7
14	18:42:54.02	-04:02:28.0	1.16	2.2	0.10	18	—	—	92	2.1	—	—
15	18:42:54.24	-04:00:16.0	1.08	2.0	0.10	18	—	—	83	1.9	—	—
16	18:42:54.77	-04:00:11.8	1.02	4.5	0.15	18	—	—	190	1.8	—	—
17	18:42:50.51	-04:00:01.5	0.83	1.1	0.08	17	—	—	47	1.5	—	—

Notes: <sup>a</sup> Significant free-free contribution (Fig. 2), with no mass and column density estimates.

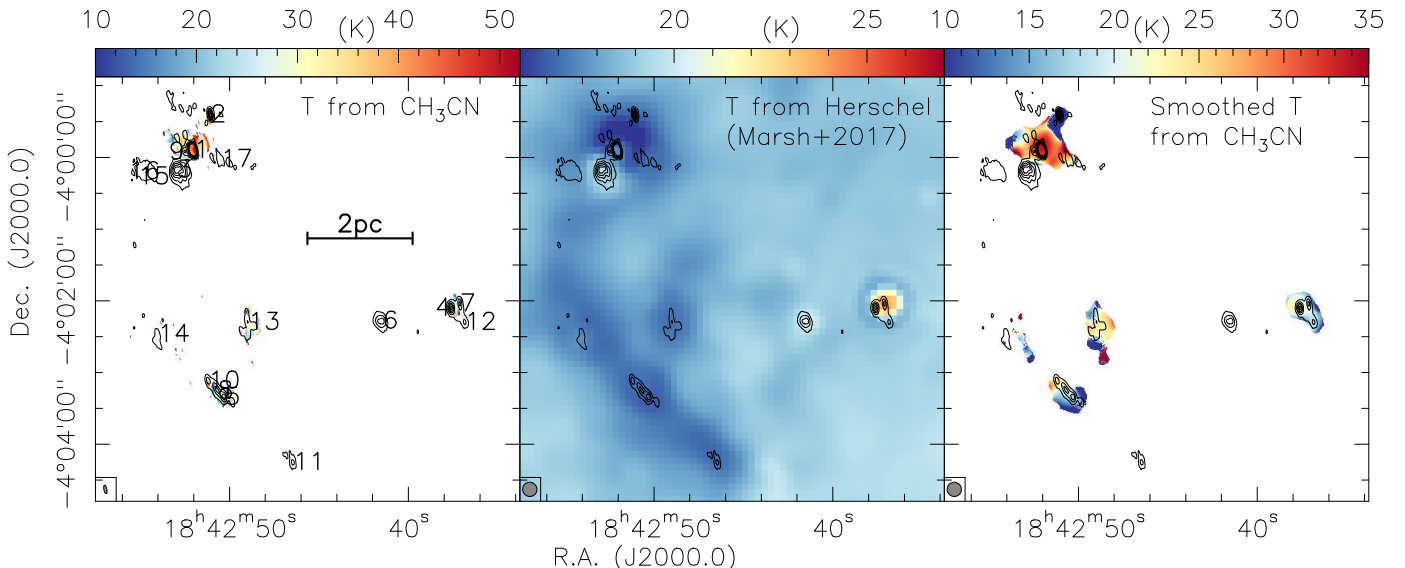


**Fig. 4.** Temperature maps. Left: Temperature map from combined fitting of  $\text{CH}_3\text{CN}(5_k - 4_k)$  and  $(4_k - 3_k)$   $k$ -ladders ( $k$  from 0 to 4). Middle: Dust temperature map from Herschel far-infrared data (Marsh et al., 2017). Right:  $\text{CH}_3\text{CN}$  temperature map, smoothed to the same 12'' spatial resolution of the Herschel map. The contours outline the NOEMA 3.6 mm continuum emission; contour levels are from 0.4 to 1.6 mJy beam $^{-1}$  ( $1\sigma \sim 0.1$  mJy beam $^{-1}$ ). The source numbers and a scale bar are shown in the left panel.

toward several clumps in the region. The main strong molecular line emission structures are G28P2/IRS2 and IRAS18402-0403 in the north, G28P1/IRS1 and G28S in the south, and G28P3 in the west (see Fig. 2 for the labeling).

Zooming into smaller spatial scales with the merged NOEMA+30 m data (Fig. 5, bottom panels), the general structures are similar as expected. However, the higher angular resolution clearly reveals that most of the molecular emission in the north does not stem from the H $\alpha$  region IRAS18402-0403 but is emitted from the younger region G28P2/IRS2. The only exception in that regard is the HCN map that also shows emission around the H $\alpha$  region. Since it is more diffuse and not very peaked, that emission likely stems from the larger-scale clump environment of IRAS18402-0403.

Regarding deuterated species, although the 30 m-only data show extended  $\text{DCO}^+$  emission, the NOEMA+30 m map is

comparably noisy without strong compact emission structures. Inspecting the NOEMA-only  $\text{DCO}^+$  data reveals barely any detectable features. This indicates that  $\text{DCO}^+$  in this region is found more in the diffuse environmental gas at lower temperatures and less toward the peak-structures. For comparison,  $\text{NH}_2\text{D}$  – which was not observed with the 30 m leaving only NOEMA data – shows compact emission toward the two youngest sources G28P1/IRS1 and G28S, whereas in the north emission structures appear at the edges of G28P2/IRS2 and IRAS18402-0403. The deuterated DNC map lies between the other two; it shows substantial extended emission but also some compact structures (see also Feng et al. (2019) for a deuteration study of G28P1 and G28S).

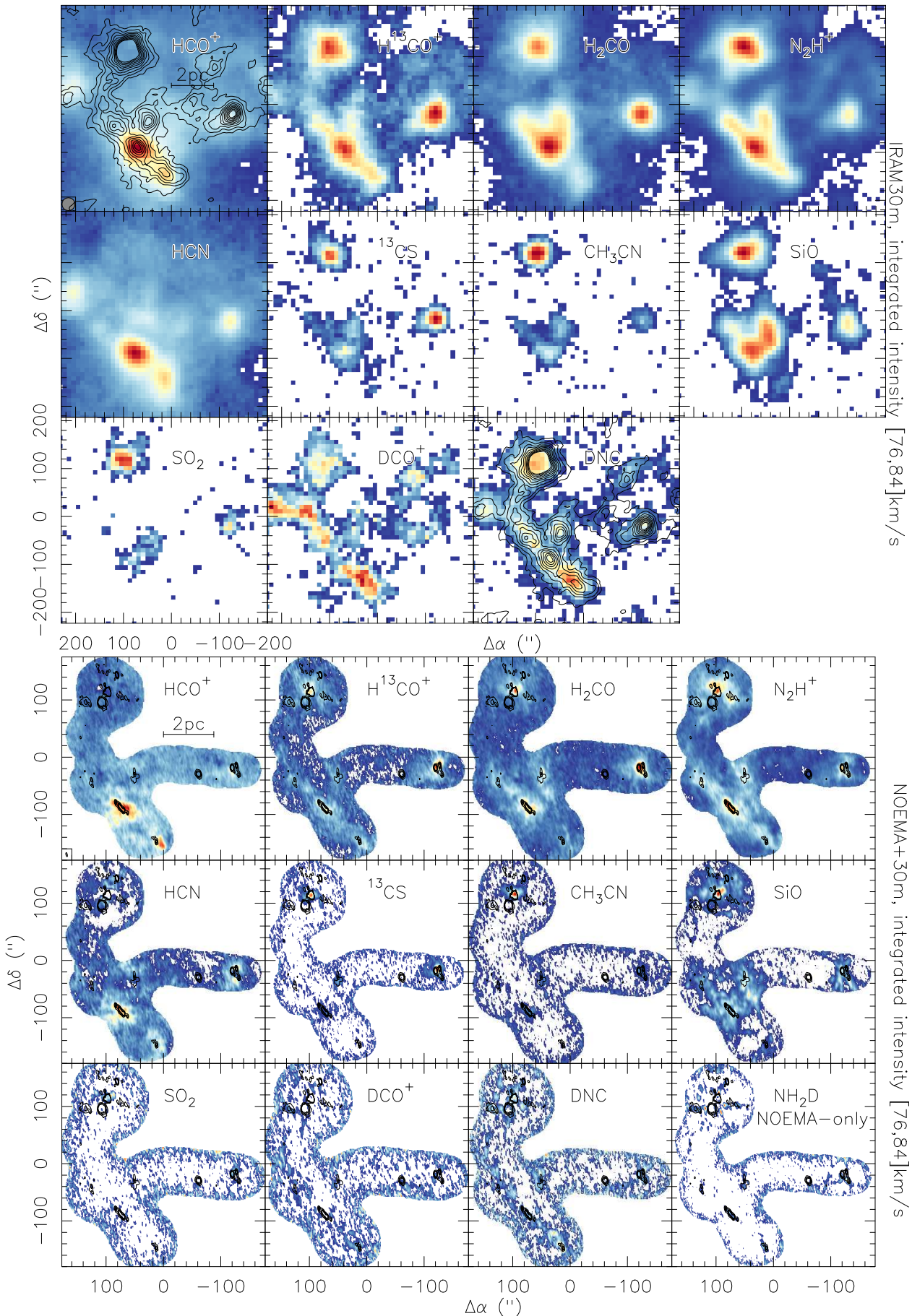


**Fig. 5.** Integrated intensity data for G28. Top: 30 m observations. Bottom: Merged NOEMA+30 m data (except  $\text{NH}_2\text{D}$ , which shows NOEMA-only data as that line was not covered by the 30 m observations). The integration range is 76 to 84  $\text{km s}^{-1}$ . All maps were created by clipping the data below the  $3\sigma$  level; intensity levels were chosen for each panel separately to better highlight the emission features. The contours on the 30 m data show  $870\text{ }\mu\text{m}$  continuum (Schuller et al., 2009) in  $3\sigma$  steps of  $0.15\text{ Jy beam}^{-1}$ . The contours on the NOEMA+30 m data show the NOEMA-only 3.6 mm continuum from 0.4 to to  $1.6\text{ mJy beam}^{-1}$  ( $1\sigma \sim 0.1\text{ mJy beam}^{-1}$ ). Molecules are labeled in all panels, and the beam and scale bar are shown in the top-left panels.

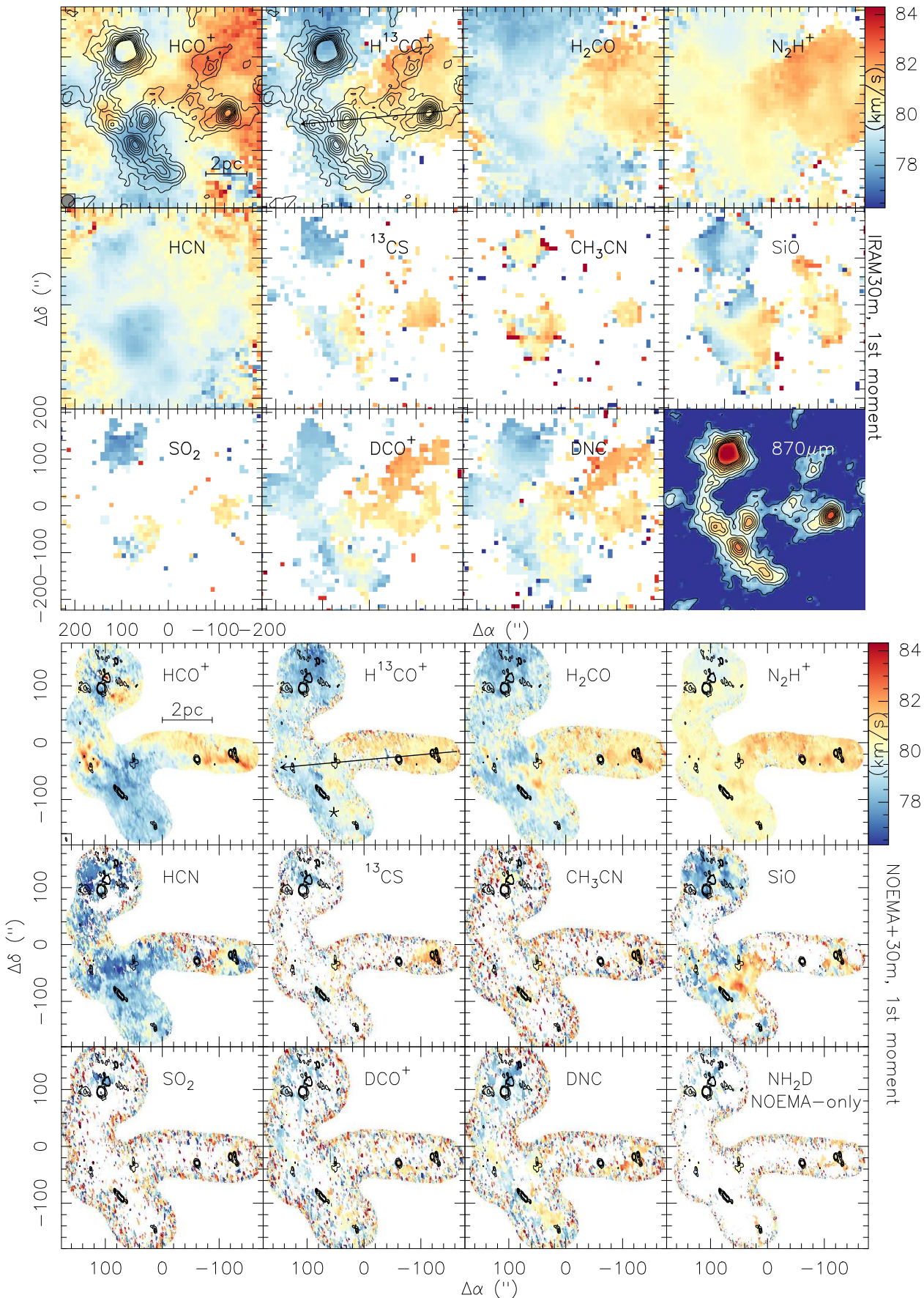


**Fig. 6.** First-moment maps (intensity-weighted peak velocities) for G28. Top: 30 m observations. Bottom: Merged NOEMA+30 m data (except NH<sub>2</sub>D, which shows NOEMA-only data as that line was not covered by the 30 m observations). All maps were created by clipping the data below the  $3\sigma$  level. The contours on the 30 m data show 870  $\mu$ m continuum (Schuller et al., 2009) in  $3\sigma$  steps of 0.15 Jy beam $^{-1}$ . The contours on the NOEMA+30 m data show the NOEMA-only 3.6 mm continuum from 0.4 to to 1.6 mJy beam $^{-1}$  ( $1\sigma \sim 0.1$  mJy beam $^{-1}$ ). Molecules are labeled in all panels, and the beam and scale bar are shown in the top-left panels. The H<sup>13</sup>CO<sup>+</sup> panels outline the west-east pv cut presented in Fig. 7.

The shock tracer SiO is an interesting additional line that traces both compact and extended emission but in a much wider velocity regime. We revisit this in the following section.

### 3.3. Kinematic properties

For our kinematic analysis, Fig. 6 presents the first-moment maps or intensity-weighted peak velocity for the same molecular lines analyzed previously in the integrated emission maps. Again we show the 30 m only data as well as the merged NOEMA+30 m data (top and bottom panels of Fig. 6). All data consistently show a velocity gradient from redshifted gas in the west to more blueshifted gas in the east. Setting that velocity gradient in relation to previous larger-scale work, this corresponds to the velocity gradient observed, for example, in  $^{13}\text{CO}$ (3–2) from high to low Galactic latitudes in Fig. 1 (Beuther et al., 2020). This west-east velocity gradient is visible in the extended 30 m-only data as well as on the small scales in the combined NOEMA+30 m data. While the velocity gradient is visible across the entire map in the single-dish data (Fig. 6), for the NOEMA high-resolution observations, we focused only on the central west-east filament with the highest column densities. The velocity ranges of the gradients appear slightly broader in tracers of comparably lower density gas such as  $\text{HCO}^+$  compared to higher-density tracers such as  $\text{N}_2\text{H}^+$  (Table 1).

To get a better understanding of the velocity structures, we created position-velocity (pv) cuts from west to east for the merged NOEMA+30 m data in the  $\text{HCO}^+$  line, its  $^{13}\text{C}$  isotopolog, and SiO. The exact outline of these pv cuts is shown in the  $\text{H}^{13}\text{CO}^+$  panels of Fig. 6. These high-resolution pv diagrams can be directly compared to the larger-scale pv structure derived for the [CI] and  $^{13}\text{CO}$ (3–2) emission in Beuther et al. (2020). Figure 7 presents a compilation of these new and old data. While the previous single-dish larger-scale observations cover an extent of more than  $10'$  across the main filament, our new NOEMA+30 m high-resolution data are more restricted and cover the gas flow from the west toward the main filament and slightly beyond. Fig. 7 (top-right panel) outlines the different extents of the pv cuts. While our new data do not cover the entire extent of the blueshifted gas flow from the east (or low latitudes in the top-left panel of Fig. 7), it nevertheless captures the convergent parts around the main west-east filament (or high to low Galactic latitudes).

The new high-resolution, high-density data now reveal interesting new kinematic information. While the lower-density tracer  $\text{HCO}^+$  ( $n_{\text{eff}} \sim 500 \text{ cm}^{-3}$ ) indeed shows blue- to redshifted gas between  $\sim 70$  and  $\sim 90 \text{ km s}^{-1}$  (Fig. 7, bottom-middle panel), its higher-density tracing  $^{13}\text{C}$  isotopolog  $\text{H}^{13}\text{CO}^+$  ( $n_{\text{eff}} \sim 2.2 \times 10^4 \text{ cm}^{-3}$ ) covers a much narrower velocity regime between  $\sim 77$  and  $\sim 93 \text{ km s}^{-1}$  (Fig. 7, bottom-left panel). Combining these two isotopologs into one panel (Fig. 7 bottom-middle panel), the  $^{13}\text{C}$  isotopolog is stronger closer to the  $v_{\text{lsr}}$  where the main isotopolog becomes optically thick. In addition to the main flow signatures from red- to blueshifted gas from east to west,  $\text{HCO}^+$  also traces comparably high-velocity gas toward all major sources and in the region. These are signatures of the molecular outflows likewise visible in the SiO emission (Fig. 7, bottom-right panel).

Narrow linewidth SiO emission has in the past been suggested as a potential tracer of low-velocity shocks from potential converging gas flows (e.g., Jiménez-Serra et al. 2010; Cosentino et al. 2020). As visualized in the SiO pv cut (Fig. 7 bottom-right panel), SiO does not show significant narrow linewidth emission along the pv cut, but only broad linewidth emission toward

the three main sources along its cut. These broad linewidths are likely caused by the many molecular outflows known in the region (e.g., Kong et al. 2019). The same general SiO linewidth structure can also be seen in the second-moment maps (intensity-weighted linewidths) presented in the appendix Fig. A.1.

Although outlining the many outflows in the region is not the focus of this paper, Fig. 8 presents an overlay of the red- and blueshifted SiO emission. One clearly finds high-velocity gas toward G28P2/IRS2 and G28N in the north, G28P1/IRS1 in the center of the filament, and G28P3 at the western end of the map. No high-velocity gas is identified toward the more evolved HII regions IRAS18402-0403 and G28fil. Interestingly, our data also do not recover the outflow known from the youngest regions G28S in the south of the filament (Feng et al., 2016; Tan et al., 2016). This non-detection in our data is most likely caused by the region being the youngest and weakest combined with our data's lower sensitivity and angular resolution compared to the previous detections mentioned.

### 3.4. Gas flow parameters

While other origins such as rotation could in principle also create red- or blueshifted kinematic signatures, for G28, we interpret the east-west velocity structure as arising from converging gas flows. The main argument stems from the previous larger-scale analysis from Beuther et al. (2020) where the [CI] pv diagram is reproduced in Fig. 7 (top-right panel). This larger-scale pv diagram clearly shows two separate velocity components – blueshifted to the east and redshifted to the west – that only merge at the position of the central north-south gas filament (longitudinal structure in Galactic coordinates). Rotational signatures would produce a smooth velocity gradient, whereas G28 clearly exhibits separate velocity structures favoring the converging flow interpretation. Also, numerical experiments typically indicate that rotation is not dominant on these scales in turbulent flows (e.g., Smith et al. 2016). Moreover, recent 3D dust studies of nearby regions found that motions in the past attributed to rotation rather result from flow convergence (Soler et al., 2013).

While the general west-east velocity gradient across the IRDC covers the entire main north-south filament (Fig. 6), in the following we focus our analysis on the west-east filamentary structure, which is clearly visible in the (sub)millimeter continuum data. To now quantify the mass flow rate  $\dot{M}$  along the filamentary structure from west to east, we follow the approach outlined, for instance, in Kirk et al. (2013); Henshaw et al. (2014); Wells et al. (2024); Beuther et al. (2025b):

$$\dot{M} = \frac{M_{\text{fil}} \Delta v}{l_{\text{fil}}} \times \frac{1}{\tan(i)} [\text{M}_\odot \text{yr}^{-1}]. \quad (1)$$

Here,  $M_{\text{fil}}$  and  $l_{\text{fil}}$  are the mass and length of the filament;  $\Delta v$  is the velocity difference from the western end of the filament to the eastern region. The final term  $\frac{1}{\tan(i)}$  in Equation 1 shows the dependence on the inclination angle  $i$  of the filamentary structure, which is unknown in this case. Wells et al. (2024) find a spread in the flow rate distributions with inclination angle  $i$  of roughly 1 order of magnitude at full width half maximum (FWHM).

Since the NOEMA-only continuum data suffer from missing flux, we based our estimate on the single-dish ATLASGAL 870  $\mu\text{m}$  dust continuum and 30 m-only spectral-line data. Using the same assumptions, as for the total mass estimate from the

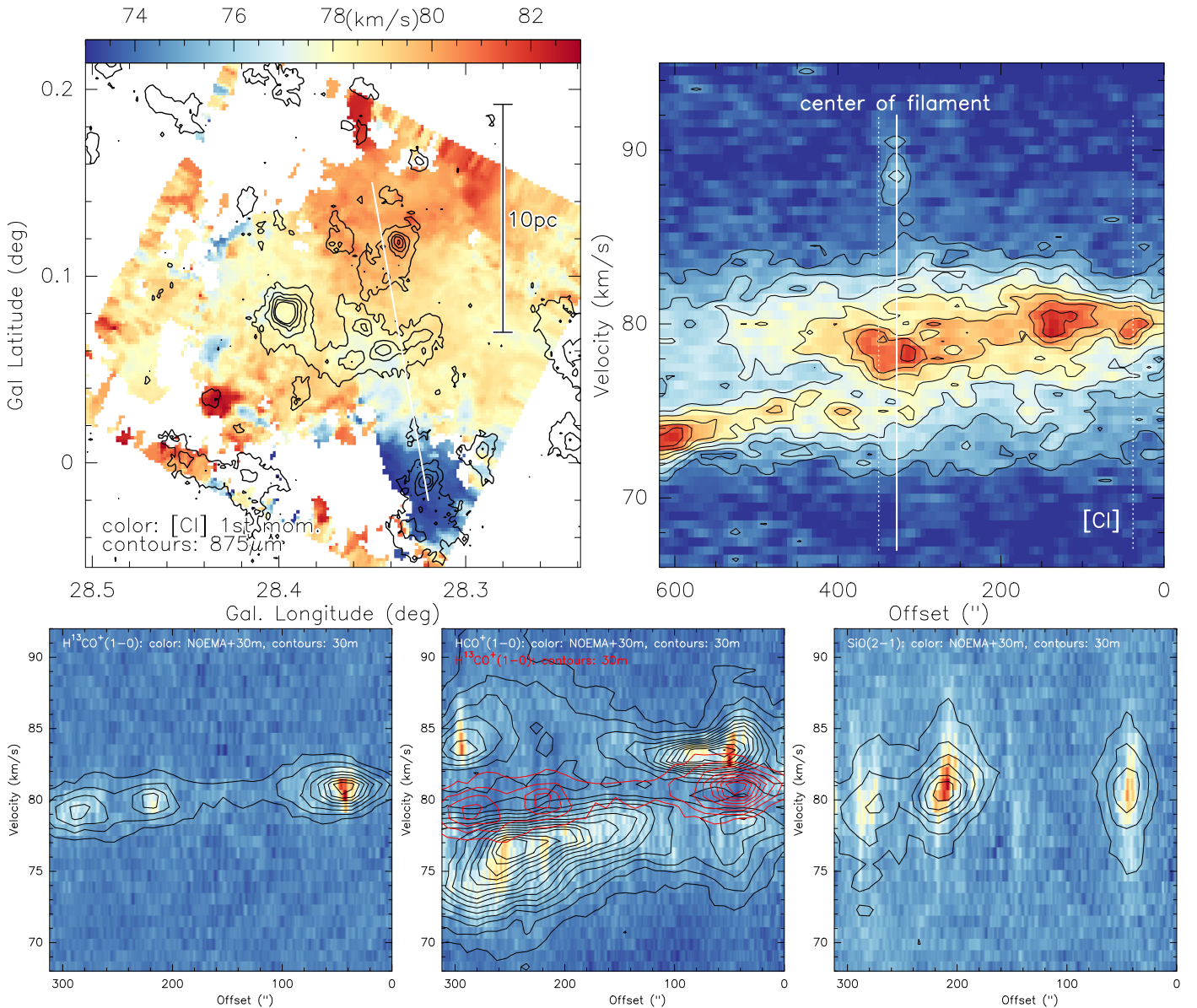


**Fig. 7.** Velocity comparison between large-scale APEX [CI] and small-scale NOEMA emission data. Top two panels: Reproduction of the [CI] first-moment map and pv cut from Beuther et al. (2020). Top-left: Color scale and contours showing the [CI] first-moment map and ATLASGAL 870 μm emission (contour levels starting at  $4\sigma$  and continuing in  $8\sigma$  steps,  $1\sigma=50 \text{ mJy beam}^{-1}$ ). A scale bar is shown as well. Top-right: Position-velocity diagram along the white arrow in the top-left panel from high to low latitudes (high latitude offset 0). The full white lines mark the center position of the single-dish filament, and the dotted lines indicate the approximate extent of the corresponding pv cuts from the NOEMA data. Bottom row: Three pv diagrams in color, with contours along the west-east line (offset 0 indicates west) shown in Fig. 6 in H<sup>13</sup>CO<sup>+</sup>, HCO<sup>+</sup>, and SiO. The color scale shows the corresponding NOEMA+30 m data, and the contours show the 30 m data only. The red contours in the middle HCO<sup>+</sup> panel also show the corresponding H<sup>13</sup>CO<sup>+</sup> emission (30 m-only data). Contour levels are in  $4\sigma$  steps.

ATLASGAL data in Sect. 3.1, we can estimate the mass in the entire west-east filament (Fig. 2) to roughly  $4014 \text{ M}_\odot$ . With a length of the corresponding pv cut (Fig. 6) of  $312''$ , corresponding at a distance of  $4.7 \text{ kpc}$  to  $\sim 7.1 \text{ pc}$ , a velocity difference in the H<sup>13</sup>CO<sup>+</sup> data of  $\sim 2 \text{ km s}^{-1}$  (from  $81$  to  $79 \text{ km s}^{-1}$ , Fig. 7 bottom-left panel), and an assumed inclination angle of  $i = 45 \text{ deg}$ , the approximate mass flow rate along that filament is  $\sim 1.15 \times 10^{-3} \text{ M}_\odot \text{ yr}^{-1}$ . While inclination uncertainties can affect the flow rate (e.g., Wells et al. 2024), we consider this flow rate as an upper limit because it assumes all gas flows toward the central filament. However, sources along the west-east structure may already gather some of the material along the way. Nevertheless,

order-of-magnitude-wise, such flow rate values appear plausible given that they feed a whole high-mass star-forming region expected to form a massive cluster in the future. We discuss that more in context in Sect. 4.1.

A different way to investigate potential flow and infall motions is via the classical asymmetric blue-skewed line profiles of optically thick lines with respect to corresponding more Gaussian optically thin counterparts (e.g., Myers et al. 1996; Mardones et al. 1997; Evans 1999; De Vries & Myers 2005; Mottram et al. 2017; Beuther et al. 2025a). While the gas flow motions discussed so far largely correspond to motions along the filamentary structures and in the plane of the sky (depend-

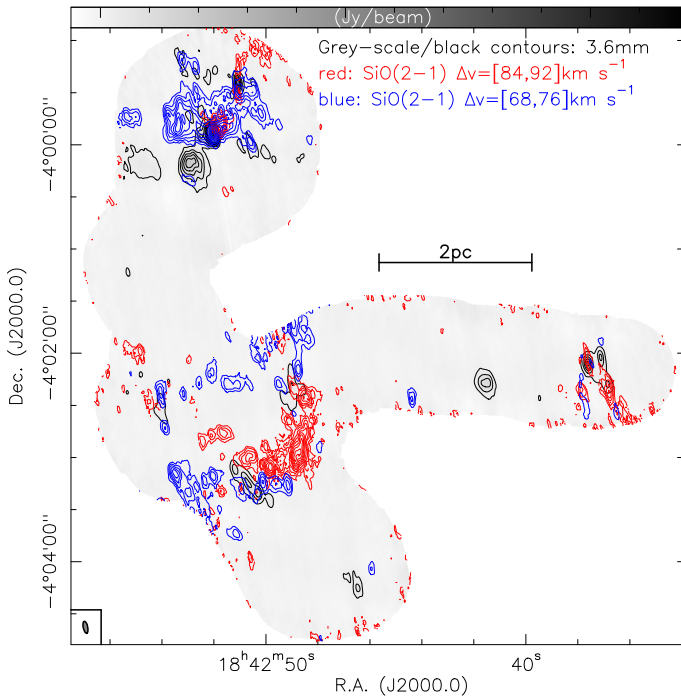


**Fig. 8.** High-velocity SiO(2-1) emission. The gray scale and contours show the 3.6 mm continuum emission, as in Fig. 3. The red and blue contours show high-velocity SiO(2-1) emission with redshifted gas between 84 and 92 km s<sup>-1</sup> and blueshifted gas between 68 and 76 km s<sup>-1</sup>, both in relative contour levels from 15 to 95% of the integrated peak emission in 10% steps. A linear scale bar and the continuum synthesized beam are shown as well.

ing on the inclination angle  $i$ , eqn. 1), the motions studied with the spectral profiles correspond to those along the line of sight. Considering the general velocity gradient in the west-east direction, we now investigate the gas motions along the line of sight onto that structure. While we use the term “flow” for the west-east gas stream, in the following, we use the term “infall” for the gas motions along the line of sight. The top panel of Fig. 9 shows a zoom-in on this west-east filament in the H<sup>13</sup>CO<sup>+</sup> first-moment map and the 3.6 mm continuum emission. We selected nine positions along the pv cut, alternating between positions offset from sources and positions toward sources. In addition, we looked at spectra 10'' north and south of the main pv cut. All these 27 positions are marked by stars in Fig. 9. The three lower spectral panels in Fig. 9 present the corresponding HCO<sup>+</sup> and H<sup>13</sup>CO<sup>+</sup> spectra for these 27 positions (the top, middle, and bottom rows correspond respectively to the north, central, and south positions marked in the top panel). We selected the main isotopolog HCO<sup>+</sup> as the optically thick tracer and its <sup>13</sup>C isotopologs as its optically thin counterpart.

In the picture of the asymmetric line profiles, blue-skewed profiles of the optically thick line indicate infall motions (see Figs. 5 and 6 in Evans (1999) for an intuitive explanation). If one now inspects the spectra along the pv cut in Fig. 9 (middle row), one sees that these spectra are dominated by blue-skewed structures. In particular, the spectra extracted toward the intermediate positions offset from the sources largely exhibit the blue-skewed signature. This is different than the on-source positions toward sources 14, 6, and 4 (from east to west) where the profiles are rather red-skewed and can be interpreted as outflow motions. This makes sense for sources 14 and 4, which are

known to drive molecular outflows visible in the high-velocity SiO emission (Fig. 8). Source 6 (or G28fil) is different since it already hosts a small HII region and is hence likely to have terminated any infall or accretion process. Therefore, we do not expect to see any infall motions toward the sources driving outflow and hosting the HII region. An interesting case is also exhibited by the spectra toward source 13, which indeed show the blue-skewed infall signature while simultaneously driving an outflow as visualized in the SiO emission (Fig. 8). In the infall picture, the outflow can lie nearly in the plane of sky without affecting the line-of-sight signatures too much. Regarding the off-source positions, only that between sources 6 and 4 shows clear red-skewed profiles.

If one leaves the central cut but moves 10'' to the north and south (Fig. 9, top and bottom spectral rows), one also identifies a clear dominance of the blue-skewed infall-indicating profiles. Altogether, these spectral structures strongly indicate infall motions toward the west-east filamentary structure.

To quantify these infall motions along the line of sight, we can follow the classical two-layer model described originally in Myers et al. (1996). This model assumes two gas layers of equal temperature and velocity dispersion  $\sigma$  that collapse toward a central region. The front and back layers correspond to the red- and blueshifted gas. Following their equation 9, one can estimate the infall velocity  $v_{\text{in}}$  as

$$v_{\text{in}} \approx \frac{\sigma^2}{v_{\text{red}} - v_{\text{blue}}} \ln \left( \frac{1 + eT_{\text{BD}}/T_{\text{D}}}{1 + eT_{\text{RD}}/T_{\text{D}}} \right), \quad (2)$$

where  $v_{\text{red}}$  and  $v_{\text{blue}}$  correspond to the red- and blueshifted peak positions,  $T_{\text{D}}$  is the intensity at the position of the dip, and  $T_{\text{RD}}$  and  $T_{\text{BD}}$  are the intensity differences between the red- and blueshifted peaks and the dip in the spectra. Using the spectral parameters measured in H<sup>13</sup>CO<sup>+</sup> and HCO<sup>+</sup> toward source 13 (fourth spectrum from the left in the middle row of Fig. 9, Table 3), we infer an infall velocity  $v_{\text{in}}$  of  $\approx 0.11$  km s<sup>-1</sup>. For comparison, the thermal sound speed of the molecular gas at 20 K of  $\approx 0.27$  km s<sup>-1</sup> corresponds to a thermal FWHM linewidth of H<sup>13</sup>CO<sup>+</sup> at 20 K of  $\approx 0.17$  km s<sup>-1</sup>. Hence, the inferred infall velocity along the line of sight toward this source is subsonic.

**Table 3.** Infall parameters

#	$\Delta v$	$v_{\text{blue}}$	$v_{\text{red}}$	$T_{\text{B}}$	$T_{\text{R}}$	$T_{\text{D}}$	$v_{\text{in}}$	$\dot{M}_{\text{in}}$
	km s	km s	km s	Jy beam	Jy beam	Jy beam	km s	$10^{-4} M_{\odot}$ yr
13	2.2	77.0	86.7	0.117	0.042	0.018	0.11	0.45
8	2.6	77.9	85.1	0.622	0.062	0.003	0.38	2.7
11	3.0	78.7	82.7	0.499	0.052	0.023	1.01	4.9

Notes: The value  $\Delta v$  represents the FWHM from H<sup>13</sup>CO<sup>+</sup>. All other spectral parameters are from HCO<sup>+</sup>. The values  $v_{\text{blue}}$ ,  $v_{\text{red}}$ ,  $T_{\text{B}}$ , and  $T_{\text{R}}$  represent the blue- and redshifted peak-velocities and peak intensities, and  $T_{\text{D}}$  represents the intensity at the dip-velocity.

With the estimated infall velocity along the line of sight and the previously derived column density (at 20 K, Table 2), we can also estimate an infall rate  $\dot{M}_{\text{in}}$  along the line of sight with

$$\dot{M}_{\text{in}} = N \times v_{\text{in}} \times r, \quad (3)$$

where  $r$  corresponds to the radius which we assume as the mean FWHM of the  $\sim 4.8''$  beam. With the given values (Tables 2 & 3), we infer an approximate infall rate along the line of sight  $\dot{M}_{\text{in}}$  of  $\approx 4.5 \times 10^{-5} M_{\odot} \text{yr}^{-1}$  for source 13. This infall rate along the line of sight is roughly a factor of 25 lower than the flow rate

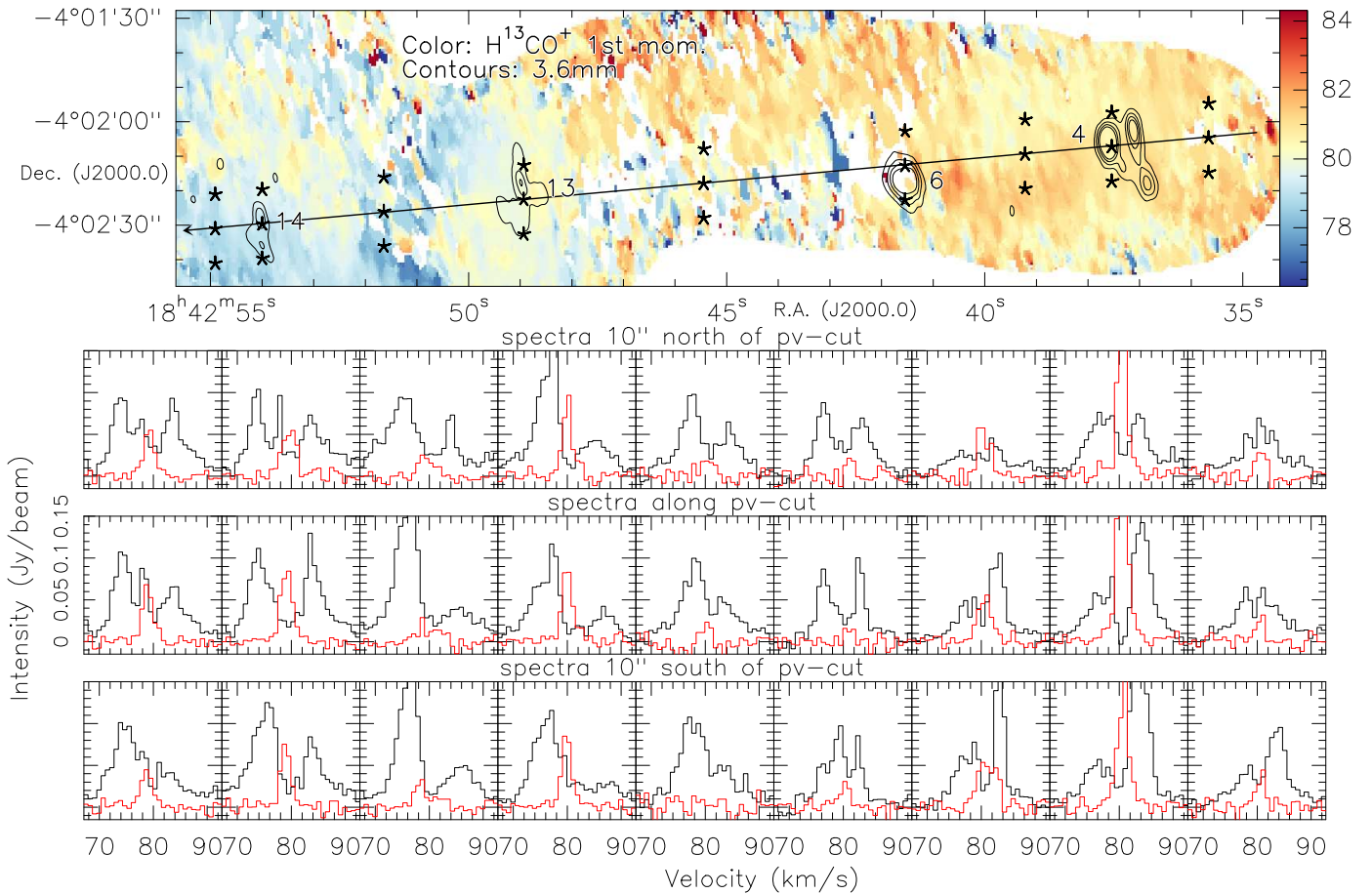


**Fig. 9.** Spectra along the west-east filament. Top: Finding chart with a color scale showing the  $\text{H}^{13}\text{CO}^+$  first-moment map and contours showing the 3.6 mm continuum in  $4\sigma$  steps. The arrow indicates the pv cut from Fig. 7; the stars mark the positions where the spectra are extracted; and the main sources are labeled (see Fig. 3). Bottom: Corresponding  $\text{HCO}^+$  and  $\text{H}^{13}\text{CO}^+$  spectra in black and red, respectively.

along the west-east filamentary structure estimated above. This large difference provides additional evidence that the gas flow is indeed dominated by a west-east converging gas flow, with much smaller flow contributions along the line of sight.

In addition to the flow and infall velocities associated with the west-east filamentary structure, we can also estimate the infall velocities  $v_{\text{in}}$  and infall rates  $\dot{M}_{\text{in}}$  for a few other regions – in particular, the two prominent star-forming regions G28P1 (source 8) and G28S (source 11) along the prominent north-south filament. Figure A.2 presents the corresponding  $\text{HCO}^+$  and  $\text{H}^{13}\text{CO}^+$  spectra, which show the blue-skewed spectra indicative of infall. Deriving the spectral parameters (Table 3), the estimated infall velocities and infall rates are all higher than those measured toward source 11 along the west-east filament. More precisely, we find  $v_{\text{in}}$  and  $\dot{M}_{\text{in}}$  toward G28P1 and G28S of  $0.38/1.01 \text{ km s}^{-1}$  and  $2.7 \times 10^{-4}/4.9 \times 10^{-4} \text{ M}_\odot \text{yr}^{-1}$ , respectively. This implies that the infall velocities toward these sources are rather supersonic. Furthermore, infall rates along the line of sight in the prominent north-south filament appear roughly 1 order of magnitude greater than those along the converging west-east flow filament. We discuss this in more detail in Sect. 4.1.

## 4. Discussion

### 4.1. Flow rates

Aiming to better understand the converging gas flow leading to the prominent G28 IRDC, we can now quantitatively characterize the different flow contributions. While earlier studies of the more diffuse gas on larger spatial scales (up to 15 pc) estimated large-scale flow rates on the order of a few times  $10^{-5} \text{ M}_\odot \text{yr}^{-1}$  (Beuther et al., 2020), the flow rates we now infer along the west-east filament ( $\sim 7.1$  pc length) in the dense-gas-tracing line  $\text{H}^{13}\text{CO}^+(1-0)$  are higher around  $1.14 \times 10^{-3} \text{ M}_\odot \text{yr}^{-1}$ . While these flow rates should be considered an upper limit – since sources along the filament can be fed along the flow – the higher inferred flow rate of the dense gas closer to the central infrared-dark filament should be real. While some models predict even opposite behaviors – i.e., decreasing flow-rates closer to the center because the large-scale flow can split into several small-scale flows (e.g., Padoan et al. 2020) – acceleration of gas by increased gravitational pull may also increase the flow rates, as observed here. In general, such high flow rates are reasonable since the converging gas flow appears to feed an entire infrared-dark filament and high-mass clusters typically gain most of their mass within several hundred thousands of years (e.g., Yorke & Sonnhalter 2002; McKee & Tan 2003; Kuiper et al. 2011; Bonnell et al. 2011; Rosen 2022; Oliva & Kuiper 2023).

The mass flow rates around  $10^{-3} \text{ M}_\odot \text{yr}^{-1}$  correspond to the standard deviation of mass flow rates obtained recently for the local ISM within 1.25 kpc from the Sun (Section 5.4 in Soler et al. 2025). If one assumed that the environment of G28 were similar to the local ISM (unlikely, since G28 lies in the Galactic midplane forming high-mass stars), one might conclude that G28 formed from a typical fluctuation in the interstellar flows encountered in the ISM. However, since the signatures of the large-scale gas flow presented here and in Beuther et al. (2020) clearly point to converging gas flows, we instead infer that G28 is undergoing a converging mass flow comparable to those found in the local ISM.

Focusing on the west-east filament, the flow is dominated by converging gas along that structure with a much smaller flow-rate contribution along the line of sight. This reconfirms the picture of a converging gas flow with a west-east orientation.

This differs from estimated flow rates along the line of sight in the prominent north-south filament, which should result from the west-east converging gas flow (see also Beuther et al. 2020). Toward sources at the heart of the infrared-dark cloud, in particular G28P1 or G28S, we infer mass infall rates on the order of a few times  $10^{-4} \text{ M}_\odot \text{yr}^{-1}$ . Such infall rates toward individual sources are again reasonable for the formation timescales of high-mass stars of a few hundred thousand years.

It is interesting to note that the flow rates along the line of sight differ by roughly an order of magnitude along the west-east filament compared to the values estimated toward the sources in the prominent north-south infrared-dark filament. This difference may indicate that the gas flow in the west-east direction along the converging gas flow is indeed dominated by this directional gas flow, whereas in the final formed structure – the north-south filament – the flow directions become more multidirectional. This proposed difference between flow rates in converging gas flows and those toward the final star-forming clumps needs further investigation by future studies.

#### 4.2. Decoupling of gas and dust temperatures

While the gas and dust temperatures presented in Sect. 3.1 and Fig. 4 are already required for accurate mass and column density estimates, the inferred differences between dust- and  $\text{CH}_3\text{CN}$ -derived gas temperatures is also an important topic in themselves. At the given high critical and effective densities of  $\text{CH}_3\text{CN}$  ( $\sim 10^5$  and  $\sim 4 - 7 \times 10^4 \text{ cm}^{-3}$  at 20 K, respectively; Schöier et al. 2005; Shirley 2015, Table 1), one would expect the gas and dust to be well coupled and hence at roughly the same temperature (e.g., Stahler & Palla 2005). We note that our gas temperature estimates are in qualitative agreement with the ones presented in Wang et al. (2008), who used  $\text{NH}_3$  to derive cold temperatures ( $\sim 16$  K) near G28P1/IRS1 and elevated temperatures ( $\sim 27$  K) around G28P2/IRS2. As shown in Table 2 and Fig. 4, wherever  $\text{CH}_3\text{CN}$  is detected, the inferred gas temperatures are systematically higher than the inferred dust temperatures. While the temperature differences decrease when the  $\text{CH}_3\text{CN}$  data are smoothed to the same spatial resolution (12'') as the dust temperature map, systematic differences nevertheless remain (Fig. 4). For all sources except source 7, the  $\text{CH}_3\text{CN}$ -derived temperatures remain either higher or nearly the same, with the largest difference being almost a factor of 2 for source 1 (Table 2). These differences may arise from technical factors as well as those of physical origin.

Regarding technical factors, the dust temperatures are based on Herschel far-infrared data at wavelengths longer than  $70 \mu\text{m}$ . Assuming blackbody emission, such long wavelength data are

by definition only sensitive to cold material, typically between 10 and 40 K. Temperatures barely above 50 K can be estimated with such kind of data (e.g., Marsh et al. 2017). In contrast,  $\text{CH}_3\text{CN}$  contains whole  $k$ -ladders with lines at various excitation temperatures. In the case of  $\text{CH}_3\text{CN}(4_k - 3_k)$  and  $\text{CH}_3\text{CN}(5_k - 4_k)$ , the  $k$ -lines with  $k = 0 \dots 4$  cover excitation energies from below 20 to above 100 K<sup>3</sup>. Therefore,  $\text{CH}_3\text{CN}$  is sensitive to a much broader range of temperatures. Contrary to this, since dust emission occurs at all column and volume densities, the dust temperature map in Fig. 4 covers the entire mapped area, whereas the  $\text{CH}_3\text{CN}$  is only detected toward dense sources due to its high critical density. Hence, while the dust temperature map is more useful for obtaining an overall picture of the entire region, the  $\text{CH}_3\text{CN}$  temperature maps may better represent the temperatures of the dense sources. In addition, since the dust continuum emission is sensitive to the density and temperature structure along the entire line of sight – including foreground and background – it may not reliably reflect local gas conditions (see also Feng et al. 2019).

Decoupling of gas and dust temperatures at high densities has in the past been mainly observed and discussed in the central molecular zone (CMZ) of the Milky Way (e.g., Marsh et al. 2016; Immer et al. 2016; Ginsburg et al. 2016; Krieger et al. 2017; Tang et al. 2021; Henshaw et al. 2023). The temperature differences there are slightly higher, with dust temperatures between 20–50 K and a corresponding gas temperature range of 50–100 K (Henshaw et al., 2023). In comparison, for source 1 we find a difference between gas and dust temperatures around  $\sim 2$ . For most other sources, however, the difference is typically  $\leq 10$  K (Table 2). An additional difference between the CMZ and the G28 cloud is that toward the CMZ, the gas and dust temperature differences have been observed with single-dish telescopes over comparably large spatial scales (e.g., Ginsburg et al. 2016; Immer et al. 2016), whereas in the G28 IRDC, they are rather localized around protostellar regions.

Nevertheless, a decoupling of gas and dust temperatures at high densities also appears in this prototypical IRDC, G28. Following the discussions of the temperature decoupling in the CMZ (see summary in Henshaw et al. 2023), radiative heating is inefficient due to poor coupling between radiation and gas (e.g., Clark et al. 2013; Ao et al. 2013; Ginsburg et al. 2016). The main candidates for explaining the different gas and dust temperatures are mechanical heating, i.e., transformation from kinetic to thermal energy at the end of the turbulent cascade via shocks or cosmic ray heating (e.g., Pan & Padoan 2009; Papadopoulos 2010). Studies indicate that mechanical heating appears the more likely candidate for the CMZ (e.g., Ginsburg et al. 2016; Immer et al. 2016). Temperature differences between gas and dust on core scales averaging around a factor of 1.7 have recently also been reported from the ALMA-IMF project (Motte et al., 2025).

Since the G28 IRDC formed through a converging gas flow, shocks and the conversion of kinematic flow energy into thermal energy also appear a very plausible gas heating process for this region. Nevertheless, since we do not know the cosmic ray ionization rate in G28, we cannot exclude contributions from cosmic rays to the higher gas temperatures. Most likely, a combination of both effects may explain the observed temperature differences. Future observations of the cosmic ray ionization rate in this and other regions, as well as simulations of converging flows and their associated energy dissipation and conversion processes, will help shed more light on the different processes in such typical Milky Way clouds.

<sup>3</sup> SPLATALOGUE webpage

## 5. Conclusions and summary

Observing the prototypical infrared-dark cloud G28 at a comparably high angular resolution (approximate beam size of  $4.8''$  or  $\sim 22500$  au) over large spatial scales ( $\sim 81$  pc $^2$ ) in a series of dense gas tracers and the 3.6 mm continuum emission, we can dissect the kinematic, fragmentation, and physical properties of the region in great depth. While presenting overall data from NOEMA and the IRAM 30 m observatory, we focused on the kinematic analysis of the converging gas flow and a partial decoupling of the gas and dust temperatures.

Our analysis confirms the converging west-east gas flows in many dense gas tracers, and we can quantitatively estimate a overall gas flow rate around  $\sim 10^{-3}$  M $_{\odot}$ yr $^{-1}$ . While this may represent an upper limit since some condensations along the flow potentially use up some of the gas, the flow rate along the converging gas flow is roughly a factor of 25 greater than infall rates measured in that region along the line of sight. This difference confirms the dominance of the west-east converging gas motions over gas motions along the line of sight. Interestingly, infall rates along the line of sight within the main north-south filaments are on the order of a few times  $10^{-4}$  M $_{\odot}$ yr $^{-1}$ , significantly higher than the line-of-sight infall rates estimated along the west-east gas flow. This indicates that, where the flows converge and most star formation takes place, the initially more directed converging gas flows may convert into more multidirectional infall motions.

A comparison of dust temperatures measured from Herschel far-infrared data with gas temperature estimates from our new CH<sub>3</sub>CN data reveals differences between the two. The gas temperatures are typically higher than the dust temperatures. This is surprising because the high critical densities of CH<sub>3</sub>CN ( $\sim 10^5$  cm $^{-3}$ ) lead to the expectation thermal coupling between gas and dust. These differences are partly reminiscent of the results otherwise mainly found in the CMZ of the Milky Way. Following the discussions on different gas and dust temperatures in the CMZ, mechanical heating and/or cosmic ray heating may explain the differences observed in the G28 IRDC as well. Since this IRDC results from a converging gas flow, the conversion of kinematic flow energy into thermal gas energy may indeed explain the higher gas temperatures compared to the dust temperature counterparts.

**Acknowledgements.** We thank the referee for the insightful comments improving the paper. This work is based on observations carried out with the IRAM NOEMA Interferometer and the IRAM 30 m telescope. IRAM is supported by INSU/CNRS (France), MPG (Germany) and IGN (Spain). D. S. has received funding from the European Research Council (ERC) under the European Union's Horizon 2020 research and innovation programme (PROTOPLANETS, grant agreement No. 101002188).

## References

Ao, Y., Henkel, C., Menten, K. M., et al. 2013, A&A, 550, A135  
 Ballesteros-Paredes, J., Vázquez-Semadeni, E., Palau, A., & Klessen, R. S. 2018, MNRAS, 479, 2112  
 Banerjee, R., Vázquez-Semadeni, E., Hennebelle, P., & Klessen, R. S. 2009, MNRAS, 398, 1082  
 Barnes, A. T., Liu, J., Zhang, Q., et al. 2023, A&A, 675, A53  
 Beuther, H., Bihl, S., Rugel, M., et al. 2016, A&A, 595, A32  
 Beuther, H., Kuiper, R., & Tafalla, M. 2025a, ARA&A, 63, 1  
 Beuther, H., Olguín, F. A., Sanhueza, P., Cunningham, N., & Ginsburg, A. 2025b, A&A, 695, A51  
 Beuther, H., Wang, Y., Soler, J., et al. 2020, A&A, 638, A44  
 Bonnell, I. A., Smith, R. J., Clark, P. C., & Bate, M. R. 2011, MNRAS, 410, 2339  
 Butler, M. J. & Tan, J. C. 2012, ApJ, 754, 5  
 Carey, S. J., Feldman, P. A., Redman, R. O., et al. 2000, ApJ, 543, L157  
 Churchwell, E., Babler, B. L., Meade, M. R., et al. 2009, PASP, 121, 213  
 Clark, P. C., Glover, S. C. O., Ragan, S. E., Shetty, R., & Klessen, R. S. 2013, ApJ, 768, L34  
 Cosentino, G., Jiménez-Serra, I., Henshaw, J. D., et al. 2020, MNRAS, 499, 1666  
 Csengeri, T., Bontemps, S., Schneider, N., Motte, F., & Dib, S. 2011a, A&A, 527, A135  
 Csengeri, T., Bontemps, S., Schneider, N., et al. 2011b, ApJ, 740, L5  
 De Vries, C. H. & Myers, P. C. 2005, ApJ, 620, 800  
 Draine, B. T. 2011, Physics of the Interstellar and Intergalactic Medium (Princeton Series in Astrophysics)  
 Evans, N. J. 1999, ARA&A, 37, 311  
 Feng, S., Beuther, H., Zhang, Q., et al. 2016, ApJ, 828, 100  
 Feng, S., Caselli, P., Wang, K., et al. 2019, ApJ, 883, 202  
 Gieser, C., Beuther, H., Semenov, D., et al. 2021, A&A, 648, A66  
 Gieser, C., Beuther, H., Semenov, D., et al. 2022, A&A, 657, A3  
 Gieser, C., Caselli, P., Segura-Cox, D. M., et al. 2025, A&A, 701, A165  
 Ginsburg, A., Henkel, C., Ao, Y., et al. 2016, A&A, 586, A50  
 Glover, S. C. O. & Mac Low, M.-M. 2007, ApJ, 659, 1317  
 Goldsmith, P. F., Heyer, M., Narayanan, G., et al. 2008, ApJ, 680, 428  
 Hacar, A., Alves, J., Tafalla, M., & Goicoechea, J. R. 2017, A&A, 602, L2  
 Hacar, A., Clark, S. E., Heitsch, F., et al. 2023, in Astronomical Society of the Pacific Conference Series, Vol. 534, Protostars and Planets VII, ed. S. Inutsuka, Y. Aikawa, T. Muto, K. Tomida, & M. Tamura, 153  
 Heitsch, F., Burkert, A., Hartmann, L. W., Slyz, A. D., & Devriendt, J. E. G. 2005, ApJ, 633, L113  
 Hennemann, M., Motte, F., Schneider, N., et al. 2012, A&A, 543, L3  
 Henshaw, J. D., Barnes, A. T., Battersby, C., et al. 2023, in Astronomical Society of the Pacific Conference Series, Vol. 534, Protostars and Planets VII, ed. S. Inutsuka, Y. Aikawa, T. Muto, K. Tomida, & M. Tamura, 83  
 Henshaw, J. D., Caselli, P., Fontani, F., Jiménez-Serra, I., & Tan, J. C. 2014, MNRAS, 440, 2860  
 Hildebrand, R. H. 1983, QJRAS, 24, 267  
 Ibáñez-Mejía, J. C., Mac Low, M.-M., Klessen, R. S., & Baczyński, C. 2017, ApJ, 850, 62  
 Immer, K., Kauffmann, J., Pillai, T., Ginsburg, A., & Menten, K. M. 2016, A&A, 595, A94  
 Jackson, J. M., Rathborne, J. M., Shah, R. Y., et al. 2006, ApJS, 163, 145  
 Jiménez-Serra, I., Caselli, P., Tan, J. C., et al. 2010, MNRAS, 406, 187  
 Kainulainen, J. & Tan, J. C. 2013, A&A, 549, A53  
 Kido, M., Yen, H.-W., Sai, J., et al. 2025, ApJ, 985, 166  
 Kirk, H., Myers, P. C., Bourke, T. L., et al. 2013, ApJ, 766, 115  
 Kong, S., Arce, H. G., Maureira, M. J., et al. 2019, ApJ, 874, 104  
 Krieger, N., Ott, J., Beuther, H., et al. 2017, ApJ, 850, 77  
 Kuiper, R., Klahr, H., Beuther, H., & Henning, T. 2011, ApJ, 732, 20  
 Law, C.-Y., Tan, J. C., Skalidis, R., et al. 2024, ApJ, 967, 157  
 Liu, J., Zhang, Q., Lin, Y., et al. 2024, ApJ, 966, 120  
 Mardones, D., Myers, P. C., Tafalla, M., et al. 1997, ApJ, 489, 719  
 Marsh, K. A., Ragan, S. E., Whitworth, A. P., & Clark, P. C. 2016, MNRAS, 461, L16  
 Marsh, K. A., Whitworth, A. P., Lomax, O., et al. 2017, MNRAS, 471, 2730  
 McKee, C. F. & Tan, J. C. 2003, ApJ, 585, 850  
 Möller, T., Endres, C., & Schilke, P. 2017, A&A, 59, A7  
 Motte, F., Bontemps, S., & Louvet, F. 2018, ARA&A, 56, 41  
 Motte, F., Pouteau, Y., Nony, T., et al. 2025, A&A, 694, A24  
 Mottram, J. C., van Dishoeck, E. F., Kristensen, L. E., et al. 2017, A&A, 600, A99  
 Myers, P. C., Mardones, D., Tafalla, M., Williams, J. P., & Wilner, D. J. 1996, ApJ, 465, L133  
 Oliva, A. & Kuiper, R. 2023, A&A, 669, A81  
 Ossenkopf, V. & Henning, T. 1994, A&A, 291, 943  
 Padoan, P., Pan, L., Juvela, M., Haugbølle, T., & Nordlund, Å. 2020, ApJ, 900, 82  
 Pan, L. & Padoan, P. 2009, ApJ, 692, 594  
 Papadopoulos, P. P. 2010, ApJ, 720, 226  
 Pillai, T., Wyrowski, F., Carey, S. J., & Menten, K. M. 2006, A&A, 450, 569  
 Pineda, J. E., Arzoumanian, D., Andre, P., et al. 2023, in Astronomical Society of the Pacific Conference Series, Vol. 534, Protostars and Planets VII, ed. S. Inutsuka, Y. Aikawa, T. Muto, K. Tomida, & M. Tamura, 233  
 Rathborne, J. M., Jackson, J. M., & Simon, R. 2006, ApJ, 641, 389  
 Rosen, A. L. 2022, ApJ, 941, 202  
 Schneider, N., Csengeri, T., Bontemps, S., et al. 2010, A&A, 520, A49  
 Schöier, F. L., van der Tak, F. F. S., van Dishoeck, E. F., & Black, J. H. 2005, A&A, 432, 369  
 Schuller, F., Menten, K. M., Contreras, Y., et al. 2009, A&A, 504, 415  
 Shirley, Y. L. 2015, PASP, 127, 299  
 Smith, R. J., Glover, S. C. O., Klessen, R. S., & Fuller, G. A. 2016, MNRAS, 455, 3640  
 Soler, J. D., Hennebelle, P., Martin, P. G., et al. 2013, ApJ, 774, 128  
 Soler, J. D., Molinari, S., Glover, S. C. O., et al. 2025, A&A, 695, A222

**Appendix A: Additional figures**

Stahler, S. W. & Palla, F. 2005, *The Formation of Stars* (ISBN 3-527-40559-3, Wiley-VCH)

Tackenberg, J., Beuther, H., Henning, T., et al. 2014, *A&A*, 565, A101

Tan, J. C., Kong, S., Butler, M. J., Caselli, P., & Fontani, F. 2013, *ApJ*, 779, 96

Tan, J. C., Kong, S., Zhang, Y., et al. 2016, *ApJ*, 821, L3

Tang, Y., Wang, Q. D., Wilson, G. W., et al. 2021, *MNRAS*, 505, 2392

Vázquez-Semadeni, E., Banerjee, R., Gómez, G. C., et al. 2011, *MNRAS*, 414, 2511

Vázquez-Semadeni, E., González-Samaniego, A., & Colín, P. 2017, *MNRAS*, 467, 1313

Vazquez-Semadeni, E., Ostriker, E. C., Passot, T., Gammie, C. F., & Stone, J. M. 2000, *Protostars and Planets IV*, 3

Vázquez-Semadeni, E., Palau, A., Ballesteros-Paredes, J., Gómez, G. C., & Zamora-Avilés, M. 2019, *MNRAS*, 490, 3061

Wang, K., Zhang, Q., Wu, Y., Li, H.-b., & Zhang, H. 2012, *ApJ*, 745, L30

Wang, Y., Beuther, H., Rugel, M. R., et al. 2020, *A&A*, 634, A83

Wang, Y., Zhang, Q., Pillai, T., Wyrowski, F., & Wu, Y. 2008, *ApJ*, 672, L33

Wang, Y., Zhang, Q., Rathborne, J. M., Jackson, J., & Wu, Y. 2006, *ApJ*, 651, L125

Wells, M. R. A., Beuther, H., Molinari, S., et al. 2024, *A&A*, 690, A185

Williams, J. P., de Geus, E. J., & Blitz, L. 1994, *ApJ*, 428, 693

Yorke, H. W. & Sonnhalter, C. 2002, *ApJ*, 569, 846

Zhang, Q., Wang, K., Lu, X., & Jiménez-Serra, I. 2015, *ApJ*, 804, 141

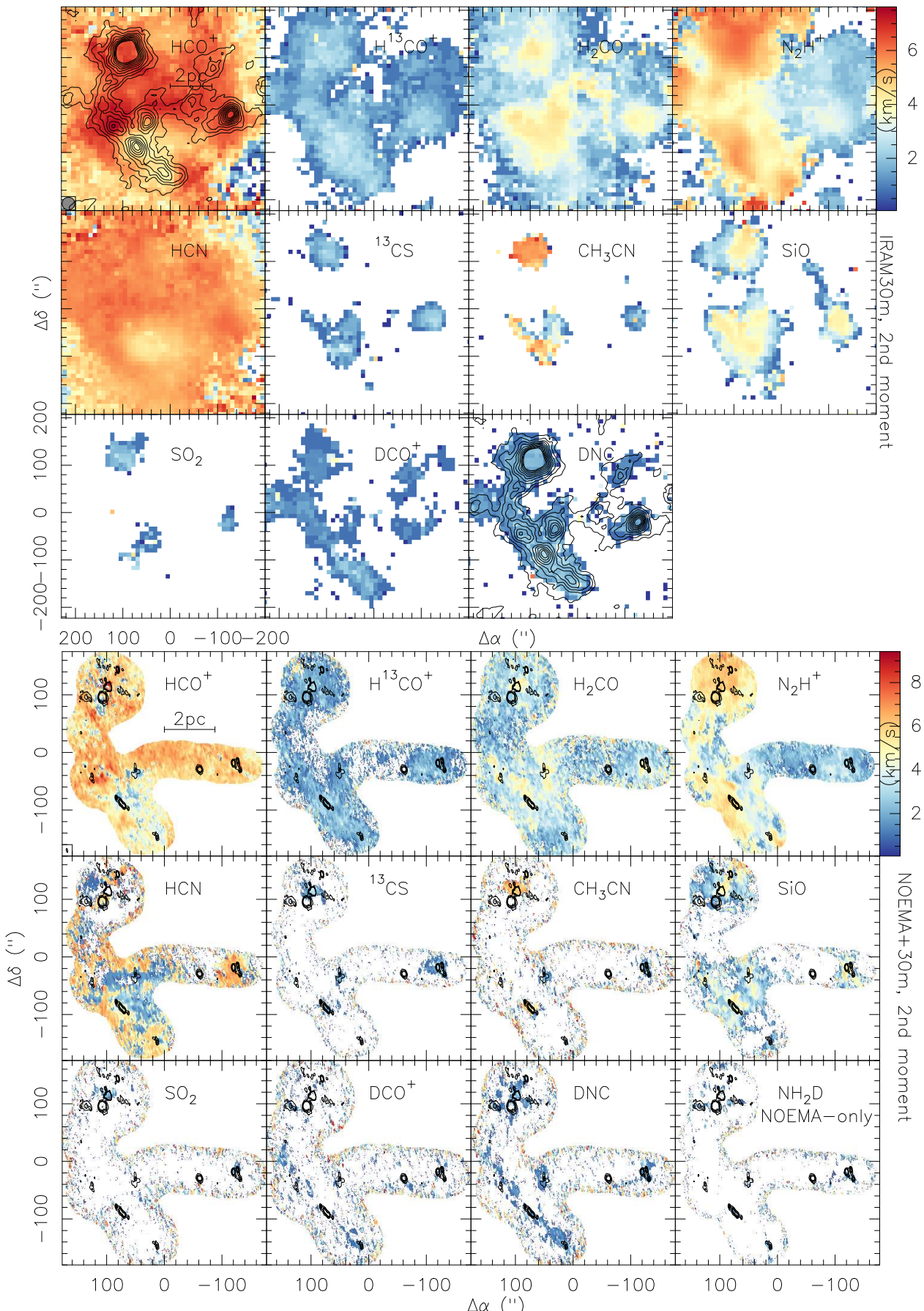


**Fig.A.1.** Second moment maps (intensity-weighted velocity dispersion) for G28. Top: 30 m observations. Bottom: Merged NOEMA+30 m data (except NH<sub>2</sub>D showing NOEMA-only data as that line was not covered with the 30 m observations). All maps were created by clipping the data below the  $3\sigma$  level. The contours on the 30 m data show 870  $\mu$ m continuum (Schuller et al., 2009) in  $3\sigma$  steps of 0.15 Jy beam $^{-1}$ . The contours on the NOEMA+30 m data show the NOEMA-only 3 mm continuum from 0.4 to 1.6 mJy beam $^{-1}$  ( $1\sigma \sim 0.1$  mJy beam $^{-1}$ ). Molecules are labeled in all panels, and the beam and scale bar are shown in the top-left panels.

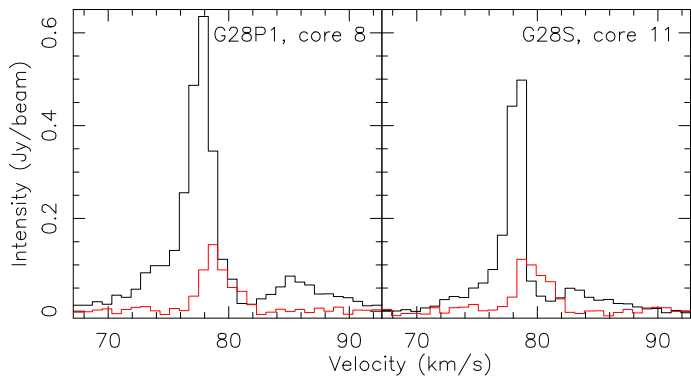


**Fig. A.2.** Spectra toward G28P1 (source 8) and G28S (source 11). Black and red correspond to the  $\text{HCO}^+$  and  $\text{H}^{13}\text{CO}^+$  spectra, respectively.